

Two-temperature relaxation and melting after absorption of femtosecond laser pulse

N. A. Inogamov^{*a}, V.V.Zhakhovskii^{b,c}, S.I.Ashitkov^b, V.A.Khokhlov^a, Yu.V.Petrov^a, P.S.Komarov^b, M.B.Agranat^b, S.I.Anisimov^a, K.Nishihara^c^aL.D.Landau Institute for Theoretical Physics RAS, Chernogolovka, 142432, Russian Federation^bJoint Institute of High Temperature RAS, 13/19 Izhorskaya street, Moscow, 125412, Russian Federation^cInstitute of Laser Engineering, Yamada-oka 2-6, Suita, Osaka 565-0871, Japan**Abstract**

The theory and experiments concerned with the electron-ion thermal relaxation and melting of overheated crystal lattice constitute the subject of this paper. The physical model includes two-temperature equation of state, many-body interatomic potential, the electron-ion energy exchange, electron thermal conductivity, and optical properties of solid, liquid, and two phase solid-liquid mixture. Two-temperature hydrodynamics and molecular dynamics codes are used. An experimental setup with pump-probe technique is used to follow evolution of an irradiated target with a short time step 100 fs between the probe femtosecond laser pulses. Accuracy of measurements of reflection coefficient and phase of reflected probe light are 1% and ~ 1 nm, respectively. It is found that, *firstly*, the electron-electron collisions make a minor contribution to a light absorption in solid Al at moderate intensities; *secondly*, the phase shift of a reflected probe results from heating of ion subsystem and kinetics of melting of Al crystal during $0 < t < 4$ ps, where t is time delay between the pump and probe pulses measured from the maximum of the pump; *thirdly* the optical response of Au to a pump shows a marked contrast to that of Al on account of excitation of d -electrons.

Key words: femtosecond laser ablation, pump-probe, optics of hot Al and Au

PACS: 52.38.Mf, 52.25.Os, 02.70.Ns

1. Supersonic heating and melting

Figures 1,2 show diagrams of processes in pump femtosecond laser pulse (fsLP) action on metal. The three time slices "ei", m_1m_2 , and c_1c_2 in Fig. 1 correspond to the following non-equilibrium processes: (e-i) the electron-ion thermal relaxation, (m) the melting of an overheated crystal lattice, and (c) the cavitation decay of a metastable state. Duration of fsLP $\tau_L \sim 40 - 100$ fs is shorter than characteristic times of these three processes. They have very various time scales from subpicoseconds to nanoseconds. The electron overheating ($T_e \gg T_i$) starts from ei_1 when a fsLP arrives [1, 2, 3, 4, 5, 6, 7, 8, 9] and disappears at ei_2 when temperatures T_e, T_i equilibrate ($t_{eq} = t_{ei2} = 3 - 6$ ps for Al at our intensities). The time is reckoned from the maximum of pump fsLP in Fig. 1. Since arriving of the pump to a target the conductivity electrons become much hotter than the ions.

Two-temperature (2T) matter with hot electrons transits to a peculiar state with thermodynamic and optical characteristics different from one-temperature (1T) case. In 2T there are appearance of excesses of electron energy and pressure above equilibrium 1T ones. Also there are changes in elastic moduli and band structure. In semiconductor lattice the binding forces become weaker with increase of T_e , while in metals situation is opposite. Large changes in optics of Au at high T_e result from

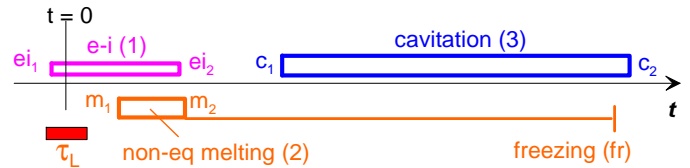


Figure 1: The pump fsLP τ_L and a chain of kinetic or transient processes (1) "ei", (2) " m_1m_2 ", and (3) " c_1c_2 " initiated by absorption of the pump.

excitation of d -electrons. On account of the ion heat capacity C_i (thermal "inertia" of a lattice) the beginning of melting $t_{m1} \sim C_i T_m / \alpha T_e$ is delayed relative to the instant "ei", where T_m and α are the melting temperature and e-i energy exchange rate.

It has been known that:

(i) for metals and semiconductors the fluences F near the ablation threshold F_{abl} are significantly higher than the melting threshold F_m [10]. In this sense the Lennard-Jones (LJ) case is an exception [10]. LJ E_m/E_{coh} vacancy migration to cohesion energy ratio and T_3/T_c triple to critical temperature ratio are large in comparison with metals and semiconductors. While E_{abl}/E_{coh} is approximately the same for all three groups. Therefore it is not surprising that in the LJ case $F_{abl} \approx F_{melt}$. In metals for $F > F_{abl}$ the molten layer is approximately as thick as heated d_T . When stretching stress overcome material strength a cavitation (fragmentation of liquid) begins inside molten metal at the instant c_1 shown in Fig. 1. In LJ near threshold $F \approx F_{abl}$ spallation (fragmentation of solid) starts in

*+7-495-7029317, Russian Federation, 142432, Chernogolovka
Email address: nailinogamov@googlemail.com (N. A. Inogamov)

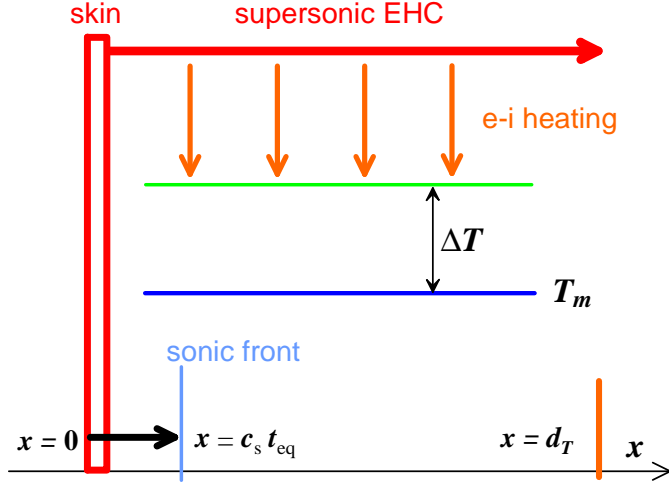


Figure 2: Electrons are heated up by a pump in a skin layer of metal (the rectangular "skin"). The "EHC" supersonically (comp. the heat d_T and sonic propagations $c_s t_{eq}$ at $t = t_{eq}$) carries heat from the "skin" layer into the bulk of the target along the horizontal arrow (it shows the heat flux) forming the heated layer d_T . The energy of hot electrons is transferred to ions in fast process of "e-i heating" (the vertical arrows) [5]. As a result the crystal lattice is overheated to ΔT above the solidus temperature. The solidus and liquidus temperatures at ρ^o are 1.2 kK, 1.48 kK (Al), 1.9 kK, 2.05 kK (Au). They are significantly higher than the melting or the triple point temperatures 933 K (Al), 1337 K (Au) corresponding to melting at low pressure.

deformed crystal [9]. Above threshold $F > F_{abl}$ the LJ spallation transforms to cavitation as molten LJ layer becomes thicker and the fragmentation zone transits from solid to molten LJ.

(ii) the electronic heat conduction wave "EHC" in Fig. 2 is *supersonic* within the 2T slice "ei" shown in Fig. 1 [5, 7].

These facts (i,ii) result in the isochoric heating and stress confinement [2, 6]. Estimates of the EHC speed are: $x_{EHC} \sim \sqrt{\chi}t$, $\chi = l\nu/3$ is a thermal diffusivity, $l = v/\nu \sim 1$ nm is a mean free path, $\nu = 1/\tau$ is a collision frequency, v is the Fermi velocity. Therefore the Mach number of EHC wave is high $\dot{x}_{EHC}/c_s \sim 100 \sqrt{\tau/t}$ up to a few picosecond. Within the time period $\sim t_{eq}$ the "EHC" creates a heated layer $d_T \approx 100$ nm thick in Al and ≈ 250 nm thick in Au [2, 3, 5, 6, 7, 9].

The d_T is much thicker than acoustic penetration depth $c_s t$ at $t < t_{eq}$ as illustrated in Fig. 2. As a result of (i) and (ii) there is a volume non-equilibrium melting in the slice "m₁m₂" [2] with formation of overheated solid grains surrounded by melt. At the slice "m₂ - fr" $t_{eq} < t < "$ fr" in Fig. 1 the heat wave velocity becomes much lower than c_s - and then the well-defined melting/recrystallization front is formed [2, 6, 11]. At $t = "$ fr" ~ 1 ns the melt layer covering a residue [12] of the target is completely solidified.

2. 2T hydrodynamics and light reflection

In Lagrangian variables the 2T hydrodynamics (2T-HD) equations [5, 6, 7, 13, 14, 15, 16, 17] are

$$\partial x(x^o, t)/\partial t = u, \quad \rho^o \partial x(x^o, t) = \rho^o \partial x^o$$

for kinematics and mass conservation,

$$\rho^o \partial u / \partial t = -\partial p / \partial x^o, \quad (1)$$

for a force balance, and two thermal equations

$$\rho^o \frac{\partial [E_e(\rho, T_e)/\rho]}{\partial t} = \frac{\partial}{\partial x^o} \left(\frac{\rho \kappa(\rho, T_e, T_i)}{\rho^o} \frac{\partial T_e}{\partial x^o} \right) - p_e \frac{\partial u}{\partial x^o} - \frac{\rho^o}{\rho} \alpha(T_e - T_i) + \frac{\rho^o}{\rho} Q, \quad (2)$$

$$\rho^o \frac{\partial [E_i(\rho, T_i)/\rho]}{\partial t} = -p_i \frac{\partial u}{\partial x^o} + \frac{\rho^o}{\rho} \alpha(T_e - T_i) \quad (3)$$

describing instant local electron and ion heat balances, where x is an Eulerian coordinate defined in Fig. 2, $x(x^o, t)$ is the trajectory of material particle with Lagrangian coordinate $x^o = x(t = -5\tau_L)$ which is equal to x before the action of a pump fsLP. In 2T-HD simulation the pump intensity is $I(t) = 0$, $t < -3\tau_L$, and $I(t) = [F/(\tau_L \sqrt{\pi})] \exp(-t^2/\tau_L^2)$, $t > -3\tau_L$; $\rho^o = \rho(x, t = -3\tau_L)$ is the initial material density: 2.71 g/cm³ (Al) and 19.3 (Au), p, ρ are pressure and density, κ is a coefficient of a thermal heat conduction. $Q(x, t) = [I(t)/\delta] \exp(-x/\delta)$, where δ is the thickness of the skin-layer shown in Fig. 2 as "skin". Unknowns ρ, T_e, T_i, u are functions of the Lagrangian variables x^o, t . When knowing the trajectories $x(x^o, t)$, the variables ρ, T_e, T_i, u can be presented as the functions of the Eulerian coordinates x, t ; E_e, E_i are the internal electron and ion energies, Q is the absorbed power, $\alpha(T_e - T_i)$ is the e-i energy exchange term.

From the profiles ρ, f, T_e, T_i , as functions of x , obtained from the Eqs.(1-3), one can find the corresponding profiles of the dielectric permittivity $\varepsilon(\rho, f, T_e, T_i) = \varepsilon_r + i\varepsilon_i$ and the complex index of refraction $N = n + ik$, $\varepsilon = N^2$, where f is a volume fraction of liquid phase discussed below for case of solid-melt mixture. Next, for the x -profile $\varepsilon(x, t_{fix})$ at fixed time t_{fix} (velocity of light is taken to be infinite), Helmholtz equation

$$\partial^2 F / \partial x^2 + \varepsilon k^2 F = 0 \quad k = \omega/c \quad (4)$$

is solved for amplitude F of the probe fsLP perpendicular to a target. Equation (4) describes a reflection of the probe light from target. Its solution gives the amplitude and phase of the reflected wave and correspondingly the time evolution $R(t), \psi(t)$ of the reflectivity R and phase ψ . They are compared with the experimental dependencies in Figs.3,4. By contrast, the pump absorption is taken from the experiment [5]. Equation (4) is evaluated by the 2×2 transfer matrices method [19]. In our experiments the chromium-forsterite laser with the pump $\lambda_{pump} = 1240$ nm and probe $\lambda_{prob} = 620$ nm (first and second harmonics) is used [5, 17]. A fsLP duration is 100 fs. Values R, ψ have been measured by microinterferometric technique described in [5, 7, 17, 20].

3. 2T thermodynamics, collisions, and thermal transport

The values $p_i, E_i(\rho, T_i)$ and $p_e, E_e(\rho, T_e)$ in (1-3) are taken as in [5] from the wide range equation of state [21] and from Fermi model for the conduction electrons, $p = p_i + p_e$ is the total pressure. The coupling factor α and the heat capacity C_e are taken from [8]. According to the Drude formula the electron heat conductivity κ in (2) is

$$\kappa = (1/3)v^2 C_e / \nu, \quad \nu = (\nu_{deg}^{-2} + \nu_{pl}^{-2})^{-1/2}, \quad (5)$$

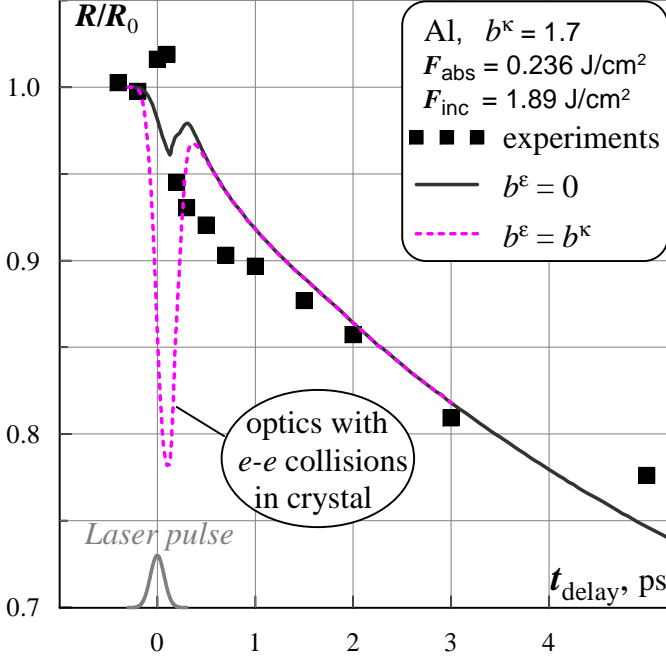


Figure 3: Role of the e-e collision frequency ν_{ee} in optics. The solid curve obtained for $\nu_{ee} = 0$. The experimental (squares) and theoretical reflectivity $R(t)$ normalized to initial R_0 of Al; $Z = 3$, $m_{eff}/m_e = 1.5$, Δ_{bb} from [18].

$\nu = \sqrt{\nu_F^2 + 3k_B T_e/m_e}$, $\nu_F = \sqrt{2E_F/m_e}$, $E_F = k_B T_F$ is Fermi energy. At $T_e < T_F$ when electron degeneracy is significant the collision frequency is $\nu \approx \nu_{deg}$ ("deg" stands for degenerate),

$$\nu_{deg} = (\nu_{ei} + \nu_{ee})(\rho/\rho^0)^{-1.3}. \quad (6)$$

The factor $(\rho/\rho^0)^{-1.3}$ in (6) approximates the quantum-mechanical molecular dynamic (MD) data [22] showing the drop of the electrical conductivity of Al with the density decrease in the temperature range under consideration. The electron-electron collision frequency is

$$\nu_{ee} = b(E_F/\hbar)(T_e/T_F)^2. \quad (7)$$

The Coulomb collisions ν_{pl} in (5) is taken as $\nu_{pl} = (E_F/\hbar)(T_e/T_F)^{-3/2}(\rho^0/\rho)^{2/3}$. They dominate at very high $T_e > T_F$ and limit ν (5) at $T \sim T_F$ by an atomic frequency $\nu_{at} \sim 10^{16} \text{ s}^{-1}$ (saturation of the ν increases with increasing T_e).

The electron-ion collisions ν_{ei} in ν_{deg} (5,6) is calculated separately for solid and liquid Al

$$\nu_{ei}^{sol} = 4.2 \cdot 10^{14}(T_i/T_3) [s^{-1}], \quad (8)$$

$$\nu_{ei}^{liq} = 1.1 \cdot 10^{14}T_i/(130 + 0.0367T_i - 66700/T_i) [s^{-1}], \quad (9)$$

where $T_3 = T_m(p = 0) = 933 \text{ K}$, T_i in K. The coefficients in (9) approximate the quantum-mechanical MD heat conduction of the molten 1T Al [23]. The thermal conductivity is calculated with Kubo-Greenwood formula up to $T = 10 \text{ kK}$ [23]. Values for κ from (5,6,8) and for electric conductivity $\sigma = n_e e^2/(m_e \nu_{ei})$ with (8) describe well 1T reference data for solid Al between the Debye and triple point T_3 temperatures.

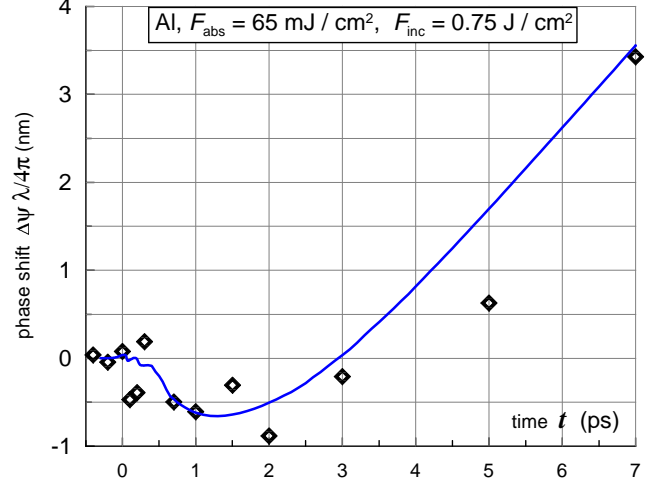


Figure 4: The drop of the phase shift $\Delta\psi$ results from the solid-liquid transition within first few picoseconds, $\Delta\psi = \psi(t) - \psi_0$, ψ_0 is an initial phase (a phase of reflected wave from a cold target). Diamonds indicate experimental data.

4. Optical properties: collisions and interband excitations

The value ε necessary for (4) is a sum of the Drude and the interband terms [4, 17, 24, 25]

$$\varepsilon = 1 - \frac{\omega_{pl}^2}{\omega^2 + \nu^2} \left(1 - i\frac{\nu}{\omega}\right) + \Delta_{bb}, \quad (10)$$

where

$$\omega_{pl}^2 = 4\pi n_e e^2/m_{eff},$$

in Al $m_{eff} = (1.2 - 1.7)m_e$. In an Al crystal Δ_{bb} results mainly from the transitions between parallel zones [18]. This term dominates at room temperatures. Its contribution increases the absorption more than by order of magnitude in comparison with pure Drude absorption. In a molten Al Δ_{bb} disappears [25]. Electron density of states (DOS) in Al is stable against melting [26] and against T_e increase as was checked up to $T_e = 70 \text{ kK}$ in [27]. Therefore the ion charge $Z = n_e/n_i$ and the electron effective mass m_{eff} defining ω_{pl} weakly depend on melting and overheating of electrons. A phenomenological dependence of Δ_{bb} (10) on a total frequency ν (5,6) has been proposed [4, 18]. At large $\nu > \omega$ the term Δ_{bb} becomes small as compared to the Drude term as it is in liquid.

5. Optics of mixtures

MD simulations show that in Al within the early (~ 0.1 - few ps) stage the solid-liquid mixture fragmentation space scale $\sim 1 \text{ nm}$ is small in comparison with δ . Therefore the ε^{mix} can be defined by a volume fraction f of liquid in mixture: $\varepsilon^{mix}(f, \varepsilon^{sol}, \varepsilon^{liq})$. For the weak mixtures ($f \approx 0$ or $f \approx 1$) we have [28]

$$\varepsilon_{f \approx 0}^{mix} = \varepsilon^{sol} \left(1 + 3f \frac{\varepsilon^{liq} - \varepsilon^{sol}}{\varepsilon^{liq} + 2\varepsilon^{sol}}\right). \quad (11)$$

An approximate interpolation for intermediate $f \sim 1$ of these linear in f solutions (11) is

$$\varepsilon^{mix} = \varepsilon_{f \approx 1}^{mix} f^4 + \varepsilon_{f \approx 0}^{mix} (1 - f^4). \quad (12)$$

Expressions (11,12) have been used in calculations shown in Figs. 3 and 4. At an early stage it is necessary to consider optics of a solid-liquid mixture given by these expressions because at this stage the thickness of a solid-liquid mixture layer is comparable with the thickness δ of a skin-layer – a penetration depth of a probe photon.

Values $\epsilon^{sol}(T = 300 \text{ K}) = -53.5 + 24.1i$, $N^{sol} = 1.6 + 7.5i$, $\epsilon^{liq}(T = 1200 \text{ K}) = -40 + 15.3i$, $N^{liq} = 1.2 + 6.4i$ [25] differ moderately. In this case there is another approximation [28]

$$(\epsilon^{mix})^{1/3} = \overline{\epsilon^{1/3}}$$

nonlinear in f but linear in small difference $\epsilon^{sol} - \epsilon^{liq}$. Comparison of this approximation with (11,12) shows that results differ small: the maximum deviation achieved at $f \approx 0.75$ is $\approx 1\%$ for $\text{Re}(\epsilon)$ and less than 3% for $\text{Im}(\epsilon)$. As was said at early stage optics of solid-liquid mixture is significant. Let us mention that as it will be shown below at this stage there is non-equilibrium melting of an overheated crystal. At intermediate and late stage c_1c_2 shown in Fig. 1 existence of vapor-liquid mixture can influence optical reflection if thickness of cavitation layer [5, 7, 14] is less or comparable with δ . The cavitation layer covers the undersurface vapor-liquid layer against probe photons.

6. Role of ν_{ee} in optics of aluminum

In an early stage the T_e is high – then the ν_{ee} (7) dominates in the total frequency ν (5) as maximum T_i for our fluences are smaller than 10 kK and the ν_{ei} collisions are less frequent. There are different coefficients b^k and b^e for the ν_{ee} (7) in expressions for κ (5) and for optics – in the Drude and in the interband terms (10). In crystals the b^k includes normal and Umklapp processes while the b^e in the solid Al may differ from zero as a result of the Umklapp effect (situation is different for gold, see below). In liquid Al the coefficient $b^e = 0$ – the e-e collisions do not contribute into optical absorption as the Umklapp is impossible. In Al a Fermi sphere is larger than in Au while the Brillouin zones are approximately equal (the lattice constants are $\approx 4 \text{ nm}$ for Al and Au both). Therefore the Umklapp effect is more significant in Al. E.g., it results in order of magnitude increase of the electron-ion energy exchange rate α [29]. Value of b in (7) is a subject of discussions. Below the Debye temperature the $\nu_{ei} \propto T^5$ tends to zero strongly and becomes less than the $\nu_{ee} \propto T^2$. Then specific electrical resistance $r = 1/\sigma$ for very pure crystals is $r = AT^2 + CT^5$. The measurements [30] give $b^e = 15$. Here we suppose that ν_{ee} does not depend on frequency of electromagnetic field and the coefficient b in (7) for resistance r is equal to b^e . At the same time the theory [30] gives $b^e = 0.6$. For high T_e the calculations [4] $b^e = b^k = 1$ is accepted.

Estimate of the upper limit for b^k follows from the check of the Wiedemann-Franz law $\kappa/\sigma = LT$ done for melt Al in [23], where L is Lorentz number. In Drude approximation we have $\kappa/\sigma = LT/(1 + \nu_{ee}^k/\nu_{ei})$ because in melt umklapp is absent and ν_{ee} (7) does not contribute to electric conductivity $\sigma = 1/r$. Relative deviation ϵ of the ratio $\kappa/(\sigma T)$ from L in [23] is less

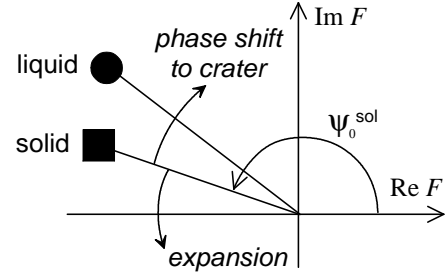


Figure 5: Deviation of a phase of reflected light resulting from melting, F is a complex amplitude of a reflected wave. $\psi_0^{sol} = \pi - 12.5 [\text{nm}]4\pi/\lambda_{prob}$ and $\psi_0^{liq} = \pi - 14.7 [\text{nm}]4\pi/\lambda_{prob}$.

than 10%. This means that electrons in Al remain degenerate up to temperature $T = 10 \text{ kK}$ achieved in [23]. The limit $\epsilon < 0.1$ impose restriction on value $b^k < 1.5 - 2$. It is obtained from $\nu_{ee}^k/\nu_{ei}^{liq} < \epsilon$ where expressions (7) and (9) was used. On the other hand, the value b^k is important at early stage because it influences heat propagation into bulk when the propagation is supersonic. To achieve thickness $d_T \approx 110 \text{ nm}$ at Al ablation threshold the values b^k should be near this restriction $b^k \approx 1.5 - 2$. The thickness $d_T \approx 110 \text{ nm}$ is necessary to reproduce experimentally defined crater depth 45 – 50 nm. For smaller b^k the simulated crater is deeper and fluence threshold is higher than the experimental ones.

Performed optical measurements shown in Figs. 3, 4 together with simulations give additional information about b^e . The interesting sharp narrow "well" at the theoretical $R(t)$ in Fig. 3 corresponds to $b^e = 1.7$. Its minimum is achieved when T_e and hence ν_{ee} (7) have the largest amplitudes (at the end of the pump). This well might be very useful for diagnostics. The left wing of the well follows the history of electron heating while the right wing reflects the kinetics of melting because the gradual phase transformation from crystal state to melt in a skin-layer progressively suppresses optical contribution of the e-e collisions (7). Unfortunately the well is not observed. Density of experimental points at the time axis in Figs. 3, 4 is large enough to exclude missing of the well between the two successive points. The accuracy of experimental measurements of a relative reflection ($\approx 1\%$) is sufficient to catch the well. Analysis of our simulation runs in a fluence range $1 < F/F_{abl} < 4$ shows that it is necessary to have the b^e below 0.2-0.5 to meet the measurements; for Al the calculated and measured thermomechanical ablation threshold is $F_{abl|inc} = 0.75 \text{ J/cm}^2$, $F_{abl|abs} = 65 \text{ mJ/cm}^2$ [5].

7. Melting and decrease of phase angle

Simulations show that the phase evolution $\psi(t)$ presented in Fig. 4 contains important information concerning the kinetics of melting. The base for this is the difference commented in Fig. 5 between the defined in Section 4 ϵ^{sol} and ϵ^{liq} . As a result of attenuation of the band-band transition during melting the value $n = \text{Re}(N)$ becomes smaller. This is why the ψ_0^{liq} in Al is 2.2 nm differing from solid in the direction of the phase rotation to the crater. The value 2.2 nm corresponds to the case

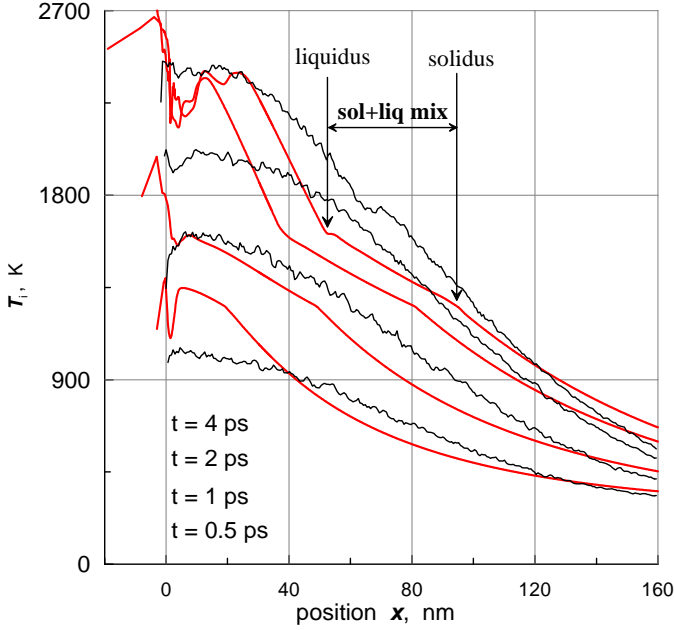


Figure 6: Rise of T_i in 2T-HD and MD (the fluctuating profiles) simulations, Al, $F_{abs} = 65 \text{ mJ/cm}^2$.

of a Fresnel reflection from homogeneous semispace. Remarkably that this small difference is measurable by the pump-probe interferometry. The sign of rotation directions in Fig. 5 defines the sign of the phase difference $\Delta\psi$ in Fig. 4. Detection of ultrafast melting of semiconductors [31] is possible due to the same liquid-solid phase difference $\Delta\psi$. But in this case the melting transforms semiconductor into a metallic state – therefore $\Delta\psi$ is significantly larger (e.g., $\Delta\psi = 12.4 \text{ nm}$ for GaAs, $\lambda = 620 \text{ nm}$) – and this transformation can be detected easily.

The phase $\Delta\psi(t)$ obtained from 2T-HD equations is compared with experimental data in Fig. 4. Expansion movement of reflecting boundary should increase $\Delta\psi$ but at the early time it decreases as a result of gradual melting of skin-layer. Agreement between data and theory indicates that theory given below properly describes the melting.

Figure 6 illustrates the heating of ions by hot electrons in 2T-HD model. In MD simulation atoms are heated by the space-time distributed thermostat power source with the temperature distribution taken from 2T-HD. This MD approach is similar to one developed in [2, 32], see also [6] where phenomenological terms describing non-equilibrium melting are added to 2T-HD equations. Particular mechanism of heating (heat flow from electrons or thermostat) has no action upon the kinetics of melting if we suppose that elastic moduli do not depend on T_e as in the case of Al [27]. In Fig. 6 the 2T-HD and MD T_i profiles are approximately the same. Some difference results from equilibrium and non-equilibrium description of melting. The arrows in Fig. 6 mark the slice of melting from equilibrium 2T-HD. The kinks at the ends of this slice result from hidden fusion energy. In MD the degradation of crystal symmetry during the fast heating and melting is distributed in wider range beyond the liquidus/solidus positions. Crystal beyond solidus is in overheated state [2, 32].

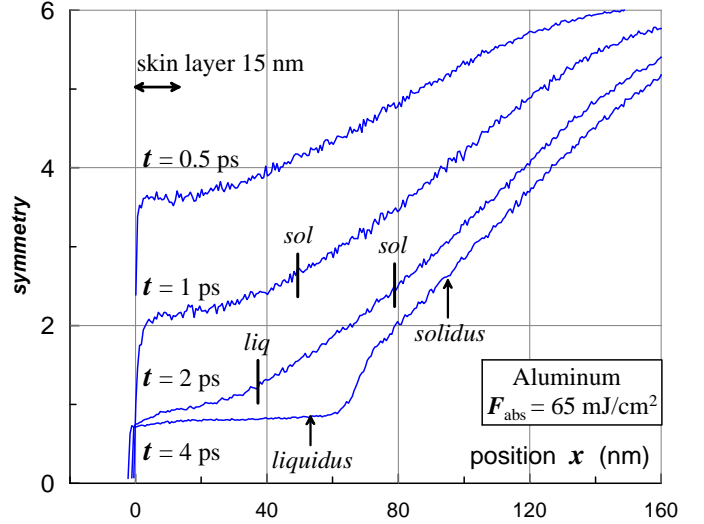


Figure 7: Evolution of the phase composition as a result of the increase of T_i . The e-i heating gradually rises T_i as it is shown in previous Figure. Transversally averaged s -profiles obtained from MD simulations are presented. The arrows "liquidus" and "solidus" at $t = 4 \text{ ps}$ are taken from previous Figure. The values of the MD symmetry index $s(x, t) = 2.5 - 2.7$ taken at the 2T-HD solidus fronts are approximately the same for different instants.

Phase transformation and propagation of melting into bulk is shown in Fig. 7. The profiles of the symmetry index s are presented. The index s is defined as a number of crystal axis passing through an atom and averaged over atoms within a x -slab, and $s = 6$ in a cold fcc lattice. One can see how quickly the rather thick (thicker than δ) layer of mixture is formed. Later the layer of pure melt (the plateau at the instant $t = 4 \text{ ps}$ s -profile in Fig. 7) appears. Much later the narrow melting front with small overheating separating a melt from a crystal is formed. Maximum thickness of the molten layer for the fluence $F_{abs} = 65 \text{ mJ/cm}^2$ is $\approx 100 \text{ nm}$.

8. Gold optical response and d -electrons

Absorption of pump fsLP causes sharp changes in optical properties at very early time – during the pulse τ_L . They are shown in Fig. 8. Bulk gold targets are used. This response is caused by fast heating of electrons. If we compare Figs. 3,4 (Al) and Fig. 8 (Au) having similar relative temperatures T_e/T_F at 2T stage and similar final $T_i = T_e$ temperatures after e-i relaxation we will see obvious large differences. They are related to the differences in the band structures of Al and Au [27]. Estimates of heating history from the maximum T_e to e-i thermalization give for the main seven thermal parameters $F_{inc}/F_{inc|abl}$, $F_{inc} \text{ J/cm}^2$, $F_{abs} \text{ mJ/cm}^2$, $E_{e|max} \text{ MJ/kg}$, $T_{e|max} \text{ eV}$, $Z = N_{e6sp}$, $T_{i|max} \text{ kK}$ the values: (0.5, 0.7, 50, 1, 1.5, 1.2, 0.8), (1, 1.3, 140, 3, 2.5, 1.5, 2.5), (2, 2.9, 500, 10, 5, 2.4, 8) for the three cases shown in Figs.8,9, where $F_{inc|abl} = (1.3 - 1.4) \text{ J/cm}^2$ is a thermomechanical ablation threshold, $E_{e|max}$, $T_{e|max}$ are electron thermal energy and temperature at the end of a pump, Z is number of electrons exited from the 5d to the 6s,6p band at the maximum $T_{e|max}$, $T_{i|max}$ is maximum ion temperature achieved after e-i relaxation. An expression

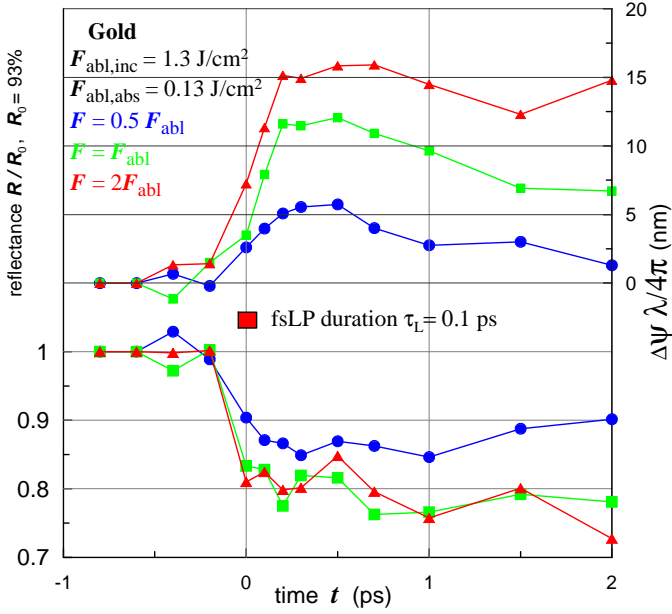


Figure 8: Sharp change of R and ψ during pump action.

$E_e(T_e) = 45.7499T_e^2 - 119.756T_e^{2.1} + 105.419T_e^{2.2} - 30.9551T_e^{2.3}$ for electron thermal energy at fixed density $\rho = 19.3$ g/cc approximates data obtained from the ABINIT [33] simulations up to $T_e = 10$ eV, here E_e is in MJ/kg, and T_e in K. Our curve is above the standard parabola $E_e = \gamma T_e^2/2$ because we include exciting of the d -electrons. But it is below the curve [8] where a red-shift of the d -band with T_e was not considered. Experimental and theoretical values for the depth of a crater at a threshold $F_{inc|abl}$ is 110 nm [7]. The first case with the smallest F_{inc} is near a melting threshold for bulk Au. Our three cases cover a range of energy densities obtained in [15, 34, 35, 36, 37] for ultrathin (25-30 nm) freestanding Au films. Here we consider bulk targets and use different technique of measurements.

The values of Z presented above have been defined using the ABINIT [33] code, the normalization condition for the number of electrons, and the expression for the amount of electrons in the 6sp band. The ABINIT has been used as in [27] for calculation of the T_e dependent DOS at different T_e supposing that density is equal to ρ^0 (isochoric heating). For given T_e the DOS of the 5d band obtained from ABINIT has been approximated by a rectangular and the DOS of the 6s,6p band has been described as the function $g(\epsilon) \propto \sqrt{\epsilon}$ in order to calculate Z . At a given T_e a root μ of the normalization condition

$$11 = \frac{\sqrt{2} m_e^{3/2} (k_B T_e)^{3/2}}{\pi^2 \hbar^3} \frac{1}{n_{atom}} \int_0^\infty \frac{\sqrt{x} dx}{e^{x-\mu/k_B T_e} + 1} + L, \quad (13)$$

where $L = (10/(E_1 - E_2)) \ln((1 + e^{(\mu - E_1)/k_B T_e}) / (1 + e^{(\mu - E_2)/k_B T_e}))$, defines a chemical potential $\mu(T_e)$, here E_1, E_2 are edges of the 5d band relative to the bottom point of the 6s,6p bands. The first and the second terms correspond to the numbers of electrons in the 6s,6p and 5d bands, resp. At room temperature these numbers are $Z = 1$ and 10. It is known that for Au difference between this approach and calculation of $\mu(T_e)$ with exact DOS is small [38]. The exact function $\mu(T_e)$ is obtained

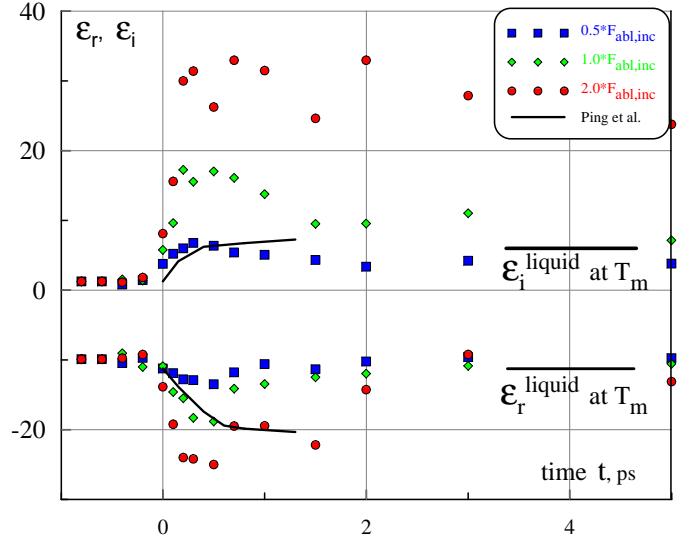


Figure 9: Fast growth of ϵ as result of electron heating. The $\epsilon = \epsilon_r + i\epsilon_i$, $\epsilon_r < 0$, $\epsilon_i > 0$ was calculated from data shown in Fig. 8 and the Fresnel formulae valid while the ϵ -profiles may be approximated by a step function. The solid curves presents data from [36] at $E_e = 2.9$ MJ/kg. They corresponds to our intermediate case $F_{inc} = F_{abl}$. Two bars give ϵ for liquid Au at 1337 K[25].

together with the DOS in the ABINIT simulation. The excitation degree Z is given by an expression $Z(T_e) = 11 - L$, where L stands for the second term in (13) but now with known $\mu(T_e)$. To estimate possible influence on the value of Z of position of the bottom point of the 6sp band this position was varied in the range ± 2 eV relative to its position at $T_e = 0$.

The values of Z and collision frequency ν are necessary for the Drude estimates of ϵ . Growth of them is responsible for the rise of $|\epsilon_r|, \epsilon_i$ in Fig. 9. At room temperature ν/ω_{prob} is small: 1.2% from electrical and thermal conductivities or 3.3% from optical data [39], $\hbar\omega_{prob} = 2$ eV. Heating of an electron subsystem in our conditions rises ν to large values: $\nu/\omega_{prob} \sim 1$. There are three candidates responsible for the growth of ν : (i) an enhancement of ν_{ei} in solid or liquid Au with $T_e \gg T_i$ in comparison with $T_e = T_i$ case, (ii) ν_{ee} and Umklapps in crystal Au, and (iii) the e-e collisions between electrons from the d and the sp bands in solid or liquid Au. Let's consider these cases.

(i) The frequency ν_{ei} and the e-i exchange rate α are coupled, $\dot{E}_{ei} = \alpha(T_e - T_i) \approx \alpha T_e \sim n_e \Delta E_{ei} \nu_{ei}(T_e)$, $T_e \gg T_i$ [40], where $\Delta E_{ei} \sim (m_e/M_i) E_F$ is an energy transfer from a light electron to a heavy ion in one e-i collision, $\nu_{ei}(T) \sim a^2(T/\theta) \sqrt{m_e/M_i}$, a is an interatomic distance in condensed matter, θ is Debye temperature. Therefore $\nu_{ei}(T_i) \sim \alpha T_i / (n_e \Delta E_{ei})$. If $\alpha = \text{const}$ as in Al [8, 29], then $\nu_{ei} = \nu_{ei}(T_i) \propto T_i$ as usual. But in gold there is significant dependence on T_e , $\alpha = \alpha(T_e)$. An approximation of calculation of $\alpha \propto \int (g(\epsilon))^2 (-\partial f / \partial \epsilon) d\epsilon$ with DOS $g(\epsilon)$ from ABINIT [33] (including the shift of the d -band with T_e) is $\alpha(T_e) = (0.23 + 4.3T_e^{3.6} / (1 + T_e^{3.5} + 0.9T_e^{4.1})) 10^{17}$ W/m³/K. It is valid up to $T_e = 10$ eV, here $f(\epsilon)$ is Fermi distribution [8]. The $\alpha(T_e)$ begins to grow at $T_e = 3$ kK from $\alpha(T_e < 3 \text{ kK}) = 0.23 \cdot 10^{17}$ W/m³/K and saturates at the

value ten times larger $\approx 2 \cdot 10^{17} \text{ W/m}^3/\text{K}$ [41]. This means that $\nu_{ei}(T_i, T_e) \sim \alpha(T_e)T_i/(n_e \Delta E_{ei})$ is enhanced if $T_e \gg T_i$, $T_e > 3 \text{ kK}$. There is $\nu_{ei}^{sol}(T) = 1.2 \cdot 10^{11} T \text{ s}^{-1}$, $\nu_{ei}^{liq}(T) = 3.3 \cdot 10^{14} + 1.5 \cdot 10^{11} T$ in 1T gold, T in K. For $T_i = 2 \text{ kK}$ we have $\nu_{ei}^{liq} = 6.3 \cdot 10^{14} \text{ s}^{-1}$. If $T_e > 2 \text{ eV}$ as in two cases shown in Figs.8,9 then the enhancement due to increase of T_e gives large frequency $\nu_{ei}(T_i = 2 \text{ kK}, T_e = 2 \text{ eV}) \sim 6 \cdot 10^{15} \approx 2\omega_{prob}$.

(ii) In Al ν_{ee}^{umkl} is small, Sec.5. As was said, the Umklapp processes are weaker in Au as the result of smaller Fermi/Brillouin ratio. Therefore it seems plausible that this candidate is less important than two other candidates.

(iii) Electrons from d versus sp bands have different angular momentum and effective mass. Therefore photons are absorbed in collisions between them. Corresponding frequency ν_{ee}^{bb} is given by (7) with possible dependence $b(T_e)$. The ν_{ee}^{bb} may be $\sim \omega_{prob}$ at $T_e \sim T_F$.

From imaginary and real parts of expression (10) we obtain $\hat{\nu} = \nu/\omega_{prob} = (\varepsilon_i - \Delta_i)/[1 - (\varepsilon_r - \Delta_r)]$ and $Z/m_{eff} = (1 + \hat{\nu}^2)(\varepsilon_i - \Delta_i)/20.6/\hat{\nu}$. The mass $m_{eff}^{Au}/m_e = 0.95 - 1.15$ at room temperatures [39] remains approximately the same with increase of T_e . This follows from our ABINIT simulations. According to [36] in 2T Au $E_d > \hbar\omega_{prob} = 2 \text{ eV}$, where E_d is an absorption edge of the d -band. If we neglect the band-band term $\Delta_{bb} = \Delta_r + i\Delta_i$ in (10), $\Delta_r = 0$, $\Delta_i = 0$, then $(Z; \hat{\nu}) = (0.9; 0.5)$, $(1.7; 0.9)$, $(3.3; 1.3)$ at the maximum $|\varepsilon_r|, \varepsilon_i$ in the three cases shown in Fig. 9.

Our data shown in Fig. 9 agree with data from [36] in ε_r but give larger ε_i and have a maximum at the time dependence $|\varepsilon_r(t)|$ while the dependence $\varepsilon_r(t)$ from [36] saturates. Perhaps the last difference results from the conductive cooling absent in ultrathin films. Let's mention that data [36] contain the useful dependence $\varepsilon(\omega)$ but may be less accurate at a particular frequency. $(Z; \hat{\nu}) = (1.2; 0.4)$ for the maximum of the dependence $\varepsilon(t)$ from [36] shown in Fig. 9 as the solid curves. As a result of smaller ε_i these values are below than our values $(1.7; 0.9)$ for the case with approximately the same energy E_e . Nevertheless there are appreciable excitation Z and frequent collisions. Therefore we can conclude that measurements confirm the theoretical findings presented above that a pump irradiation creates an excited population ($Z > 1$) rising ω_{pl} (10) and transfers gold into the state with strongly collisional widened energy levels.

The work is supported by the RFBR grant No. 07-02-00764.

References

[1] S.I. Anisimov et al., Sov. Phys.-JETP 39 (1974) 375.
[2] D.S. Ivanov, L.V. Zhigilei, Phys. Rev. B 68 (2003) 064114.
[3] P. Lorazo, L.J. Lewis, M. Meunier, Phys. Rev. B 73 (2006) 134108.
[4] D. Fisher, M. Fraenkel, Z. Henis et al., Phys. Rev. E 65 (2001) 016409.
[5] S.I. Anisimov, N.A. Inogamov et al., Appl. Phys. A 92 (2008) 939.
[6] A. Volkov, L. Zhigilei, J. Phys.: Conf. Ser. 59 (2007) 640.
[7] N. Inogamov, V. Zhakhovskii, S. Ashtikov et al., JETP 107 (2008) 1.
[8] Z. Lin, L. Zhigilei, V. Celli, Phys. Rev. B 77 (2008) 075133.
[9] S. Anisimov, V. Zhakhovskii, N. Inogamov et al., JETP 103 (2006) 183.
[10] Yu.V. Petrov et al., Proc. of SPIE 7005 (2008) 70051W-1; A.K. Upadhyay, N.A. Inogamov, B. Rethfeld et al., Phys. Rev. B 78 (2008) 045437.
[11] W. Duff, L. Zhigilei, J. Phys.: Conf. Ser. 59 (2007) 413.

[12] The cavitation or run-away layer is thermally weakly coupled with a future crater bottom and therefore may remain molten while the bottom becomes frozen. At the c_1c_2 slice in Fig. 1 the cavitation layer is mechanically coupled with the bottom through the fragmentation or nucleation zone, [5, 7, 9], Agranat et al., Appl. Surf. Sci. 253 (2007) 6276.
[13] S. Amoruso, R. Bruzzese, X. Wang et al., J. Phys. D 40 (2007) 331.
[14] S.I. Anisimov, N.A. Inogamov et al., Appl. Phys. A 92 (2008) 797.
[15] J. Colombier, P. Combis, E. Audouard et al., Phys. Rev. E 77 (2008) 036409.
[16] F. Vidal, T.W. Johnston, S. Laville, O. Barthelemy, M. Chaker, et al., Phys. Rev. Lett. 86 (2001) 2573.
[17] M.B. Agranat, N.E. Andreev, S.I. Ashtikov et al., JETP Lett. 85 (2007) 271.
[18] N.W. Ashcroft, K. Sturm, Phys. Rev. B 3(6) (1971) 1898.
[19] J. Bonse, K.-W. Brzezinka, A.J. Meixner, Appl. Surf. Sci. 221 (2004) 215.
[20] V. Temnov, K. Sokolowski-Tinten et al., J. Opt. Soc. Am. B 23 (2006) 1954.
[21] A.V. Bushman, G.I. Kanel', A.L. Ni, V.E. Fortov, Intense dynamic loading of condensed matter, Taylor & Francis Translation, 295 p., 1993.
[22] M. Desjarlais, J. Kress, L. Collins, Phys. Rev. E, 66 (2002) 025401(R).
[23] V. Recoules, J.-P. Crocombette, Phys. Rev. B 72 (2005) 104202.
[24] E.D. Palik(ed.) Handbook Opt.Const.Solids. Academic Press, N.Y., 1998.
[25] J.C. Miller, Philos. Magazine 20 (1969) 1115.
[26] M. Alemany, L. Gallego, D. Gonzalez, Phys. Rev. B 70 (2004) 134206.
[27] V. Recoules, J. Clerouin, G. Zerah et al., Phys. Rev. Lett. 96 (2006) 055503.
[28] L.D. Landau, E.M. Lifshitz, Electrodynamics of continuous media, Pergamon Press, Oxford etc., 1984.
[29] Yu.V. Petrov, Laser Particle Beams 23 (2005) 283.
[30] M. Kaveh, N. Wiser, Adv. Phys. 33(4) (1984) 257.
[31] K. Sokolowski-Tinten, J. Bialkowski et al., Phys. Rev. B 58 (1998) R11805.
[32] Z. Lin, L.V. Zhigilei, J. Phys.: Conf. Ser. 59 (2007) 11.
[33] The ABINIT code is a common project of the Universite Catholique de Louvain, Corning Inc., and other contributors (<http://www.abinit.org>).
[34] K. Widmann, T. Ao, M. Foord et al., Phys. Rev. Lett. 92 (2004) 125002.
[35] S. Mazevet, J. Clerouin, V. Recoules et al., Phys. Rev. Lett. 95 (2005) 085002.
[36] Y. Ping, D. Hanson, I. Koslow et al., Phys. Rev. Lett. 96 (2006) 255003.
[37] T. Ao, Y. Ping, K. Widmann et al., Phys. Rev. Lett. 96 (2006) 055001.
[38] Z. Lin, L.V. Zhigilei, Proc. of SPIE 6261 (2006) 62610U.
[39] P.B. Johnson, R.W. Christy, Phys. Rev. B 6 (1972) 4370.
[40] M.I. Kaganov, I.M. Lifshits, L.V. Tanatarov, Sov. Phys.-JETP 4(1957)173.
[41] This value is only 1.5 times smaller than the α_{Al} (at low T_e $\alpha_{Al}/\alpha_{Au} = 15$). May be this explains why the d_T and the crater depth at the ablation threshold differ only twice in Au versus Al. The saturation T_e is $\approx 2 \text{ eV}$.